Multi-Layered Circular Dielectric Structures' Synthetic Aperture Radar Imaging Based on Green's Function Using Non-Uniform Measurements

Baolong Wu [1,*] , **Guillermo Álvarez-Narciandi** [2] and **Jaime Laviada** [2]

[1] College of Computer Science and Electronic Engineering, Hunan University, Changsha 410082, China
[2] Department of Electrical Engineering, University of Oviedo, 33203 Gijón, Spain;
    alvareznguillermo@uniovi.es (G.Á.-N.); laviadajaime@uniovi.es (J.L.)
*   Correspondence: wubaolongyou@163.com or wubaolongyou@hnu.edu.cn

check for updates

Abstract: The electromagnetic imaging of multi-layered circular structures can be accomplished by means of different approaches. Among these approaches, the use of synthetic aperture radar (SAR) techniques with the compensation of the Green's function for multi-layered circular cylinders provides a trade-off between accuracy and computational complexity. Nevertheless, this approach relies on measurement points acquired uniformly. Thus, this prevents the adoption of more flexible sampling schemes, limiting the use of inaccurate positioners or manual scanners. To overcome this limitation, this paper proposes a method to handle non-uniform cylindrically acquired data, enabling multi-layered circular imaging based on non-uniformly acquired measurements. For this purpose, the presented method starts by projecting the non-uniformly measured points onto different circles with equally-spaced points. After that, the Green's function-based circular-SAR imaging method is applied to each projection circle. Lastly, the final SAR image is obtained by the superposition of the images from the previous step. Numerical simulations and experimental results demonstrated the effectiveness and robustness of the proposed method for practical nondestructive testing (NDT) applications.

Keywords: synthetic aperture radar; SAR; electromagnetic imaging; circular SAR; nondestructive testing

1. Introduction

In the context of airborne synthetic aperture radar (SAR) imaging systems, circular scanning (i.e., circular synthetic aperture) enables the acquisition of information from an object or a scene from multiple views (angles), resulting in the approach known as circular-SAR (C-SAR) [1–7]. In this remote sensing application, the free-space imaging background is usually assumed. Considering this assumption, many imaging approaches have been proposed based on free-space Green's function, Fourier, back-projection, and time-reversal algorithms [1,2,4–7]. However, for many practical industrial applications based on C-SAR imaging, involving nondestructive testing (NDT) of layered dielectric structures, such as pipes made of plastics, fiberglass, high-density polyethylene (HDPE), and polyvinyl chloride (PVC) that carry fluids and chemicals, this assumption no longer holds. If the free-space imaging background is assumed for these cases, the resulting image will not be properly focused, and the object of interest may not be identified.

Commonly for these applications, the geometry of the layered cylinder (i.e., radii of layers and their dielectric properties) are known. In the case of equally-spaced data but inhomogeneous media, a SAR approach based on modeling field propagation by Green's function for multi-layered geometries, implemented by efficient Wiener deconvolutions, has been demonstrated for NDT and imaging

purposes for planar media [8–10]. Later, multi-layered cylindrical media imaging based on Green's function and time-reversal approach have also been demonstrated for NDT [11,12]. For the problem of accurate computation of electromagnetic fields due to point sources (tensor Green's function) in cylindrically stratified media, a stable/robust methodology has also been developed in [13,14]. For the above multi-layered media imaging method, we need to note that it is limited to low-loss media applications because high-frequency electromagnetic waves cannot penetrate high-loss materials (such as metallic materials) effectively. For relatively high-loss materials, much lower frequencies could be used for imaging at the expense of lower resolution. Therefore, the frequency band selection should be performed, considering the tradeoff between imaging resolution and penetration capabilities and the specific requirements of the practical applications of interest.

Despite these powerful approaches for uniform data, last advances in electromagnetic imaging have shown that the use of portable scanners, driven by hand, can be useful for a large number of applications, including electromagnetic compatibility [15], people screening [16], or nondestructive evaluation [17]. However, these systems do not provide equally-spaced acquisition points. Thus, it is convenient to increase the flexibility of the sampling requirements of previous approaches in order to be ready for setups not including a fixed scanning platform. Consequently, developing a multi-layered C-SAR imaging technique with the capability to handle non-uniform measurement points becomes an important demand.

The position of the non-uniform measurement points can be recorded by means of affordable systems, such as depth-cameras [16] or motion capture systems [15,17]. Thus, the above problem becomes how to design the multi-layered C-SAR imaging algorithm once the non-uniform measurement points are known.

It is relevant to note that some flexible sampling techniques have been proposed in the past for C-SAR imaging. In this context, a time-reversal imaging technique for cylindrically multi-layered media has been proposed in [12]. Despite the flexibility of this technique, which can deal with the non-concentric cylinder and also non-uniform acquisition data, it entails a large computational burden. Moreover, it is not as accurate as the full-wave compensation achieved by compensating the Green's function, as it accounts for the infinite reflections between layers (see further details in [12]). This paper shows a novel method to solve the problem of a multi-layered C-SAR imaging algorithm based on Green's function, once the non-uniform measurement points are known.

2. Methods

2.1. Green's Function-Based SAR Imaging Method of Uniform Measurement Points for Multi-Layered Circular Dielectric Structures

As shown in Figure 1a, in a similar fashion to [11], the schematic of the uniform measurement case for three-layered circular dielectric structures was presented. The same methodology could be used when dealing with more layered dielectric models. The first layer corresponded to the background medium, which is typically air. The measurement points were located in this first layer and labeled as "▲", representing the uniform discrete measurement points. The second and third layers were the imaging domain, and they were made up of two different materials (i.e., different dielectric constants). The targets to be imaged or detected were located in the inner layer, and they were represented as "●". Therefore, the goal was to obtain the SAR image in the imaging domain based on Green's function from the monostatic scattered field, which was acquired at a set of uniform positions. The multi-layered circular dielectric imaging area could be reconstructed, according to Equation (1), based on Green's function method [11].

$$\Gamma(\rho,\phi) = \int_{\omega} \hat{\Gamma}(\rho,\phi,\omega)d\omega \tag{1}$$

where

$$\hat{\Gamma}(\rho,\phi,\omega) \approx F^{-1}\left\{\widetilde{s}\left(\rho',k_{\phi},\omega\right)\widetilde{G}^{*}_{rt}\left(\rho',\rho,k_{\phi},\omega\right)\right\} \tag{2}$$

$$\widetilde{G}_{rt}\left(\rho',\rho,k_\phi,\omega\right) = F\left\{G_{rt}(\rho',\rho,\phi,\omega)\right\} \tag{3}$$

$$\widetilde{s}\left(\rho',k_\phi,\omega\right) = F\left\{s(\rho',\phi,\omega)\right\} \tag{4}$$

where the operator F denotes Fourier transform, superscript * denotes complex conjugate, and $\hat{\Gamma}$ denotes the estimated reflectivity function. The radii of the measurement points and imaging pixels are denoted by ρ' and ρ, respectively. The variable along the angular direction and angular frequency are denoted by ϕ and ω, respectively. $s(\rho',\phi,\omega)$ denotes the echoed signal at the measurement points. G_{rt} denotes the two-way Green's function of uniform measurement points, which could be calculated in advance, once the structure of the dielectric object and the radius of the uniform measurement points are defined [11]. After $\widetilde{s}\left(\rho',k_\phi,\omega\right)$ and $\widetilde{G}_{rt}\left(\rho',\rho,k_\phi,\omega\right)$ were calculated using Equation (4) and Equation (3), respectively, then it was possible to compute $\hat{\Gamma}(\rho,\phi,\omega)$ using Equation (2). Finally, $\Gamma(\rho,\phi)$ was obtained using Equation (1).
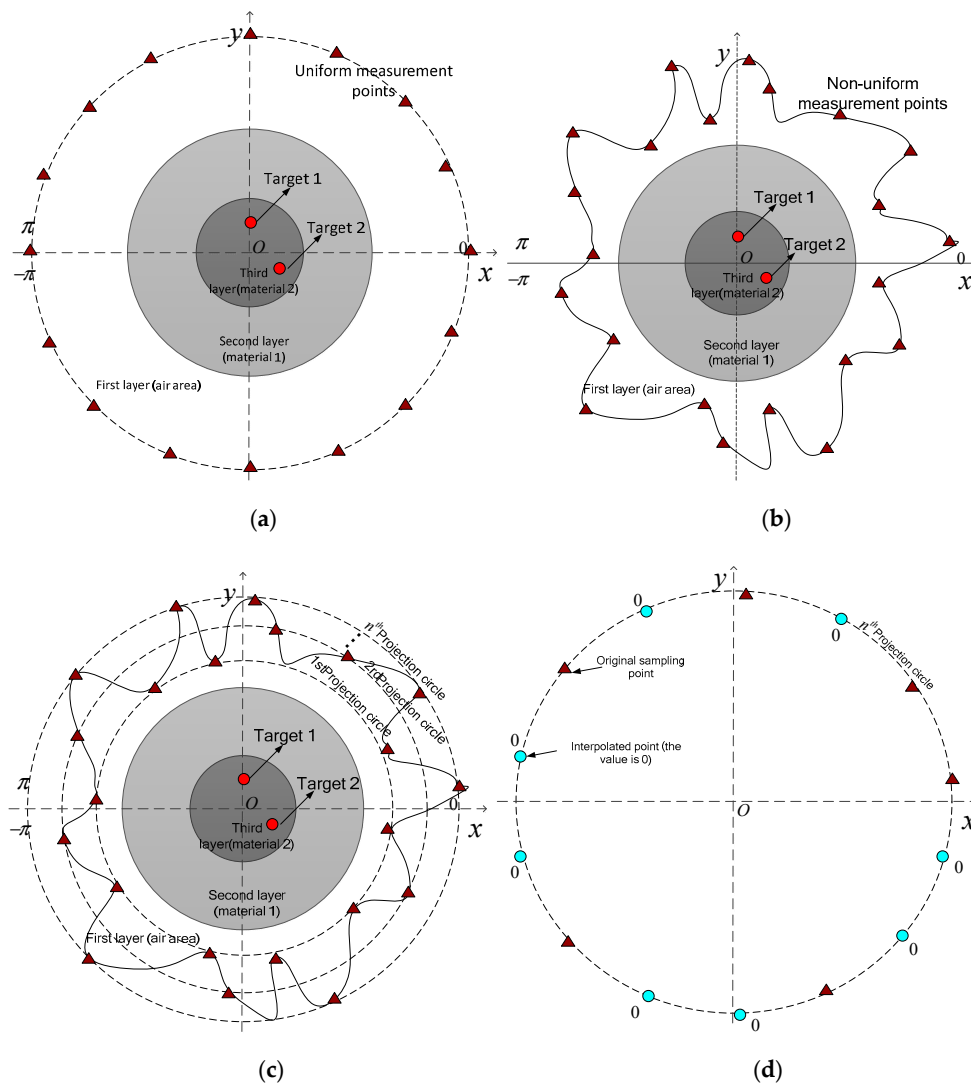

Figure 1. (a) Schematic of the uniform measurement points acquired around the three-layered dielectric object; (b) Schematic of the non-uniform measurement points acquired around the three-layered dielectric object; (c) Schematic of the projection circles for non-uniform measurement points; (d) Schematic of the interpolated points, which were set to zero, in each projection circle.

2.2. Green's Function-Based SAR Imaging Method of Non-Uniform Measurement Points for Multi-Layered Circular Dielectric Structures

In a similar fashion to Figure 1a, the schematic of the non-uniform measurement case for three-layered circular dielectric structures is presented in Figure 1b. Since the non-uniform measurement points were distributed discretely, these non-uniform measurement points could always be projected (i.e., located) onto some discrete circles, which had the same radii as the measurement points, as shown in Figure 1c. For each projection circle, it was possible to build an array of equally spaced points by complementing the real acquisition points, which were located in the aforementioned circle, with *virtual* measurement points, whose value was set to zero. These virtual points are depicted by "⬤" in Figure 1d. It should be remarked that a very small virtual angular step size could be set along each projection circle so that the projection along the angular coordinate could be achieved with arbitrary precision. Thus, the real acquisition points could be projected onto the most suitable virtual location, i.e., with the nearest distance to it. For the other virtual locations, their value was set to 0.

The first step for C-SAR imaging based on Green's function, as proposed in [11], was to calculate the discrete frequency spectrum of all of the measurement points along the measurement circle, i.e., $\widetilde{s}(\rho', k_\phi, \omega)$ in Equation (4) described in Section 2.1. This step was required as the Green's function C-SAR [11] performed the deconvolution with the Green's function in the spectral domain. According to the definition of the discrete Fourier transform (DFT), see Equation (5), the frequency spectrum was not affected by the values of the signal $x[n]$, which were zero.

$$X[k] = \sum_{n=0}^{N-1} x[n] e^{-j2\pi \frac{k}{N} n}, 0 \leq k \leq N-1,\qquad(5)$$

where $x[n]$ is the received discrete signal in the time domain, and $X[k]$ is the discrete frequency spectrum. Thus, adding the interpolated virtual measurement points to the original measurement points, as depicted in Figure 1d, did not affect the corresponding frequency spectrum, i.e., $\widetilde{s}(\rho', k_\phi, \omega)$. Considering this frequency spectrum and the corresponding deconvolution [11], i.e., Equations (4), (3), and (2) in Section 2.1, for every projection circle shown in Figure 1c, a set of complex SAR images was obtained.

Next, the complex SAR sub-images from each projection circle were coherently combined, yielding the final SAR image of the imaging domain:

$$\Gamma_{image} = \Gamma_{image,1} + \Gamma_{image,2} + \ldots + \Gamma_{image,N},\qquad(6)$$

where Γ_{image} is the final SAR image after the superposition in the complex domain of all the SAR sub-images from each different projection circle, which are denoted by $\Gamma_{image,i}$ and calculated by means of Equations (1)–(4), where the index *i* represents each different projection circle.

3. Results and Discussion

3.1. Point Spread Function (PSF) and Error Analysis

In order to characterize the theoretical performance of the method, the point spread function (PSF) was explored by conducting simulations with one ideal point target. In particular, Matlab software was used to generate the echoed signal of the point target for the non-uniform measurement points. In the simulation, 51 equally-spaced frequency points between 8.3 GHz and 12.3 GHz were considered. The radii of the outer surface (second layer) and the inner surface (the third layer) of the circular dielectric object (see Figure 1b) were set to 62.8 mm and 59.3 mm, respectively. Regarding the acquisition radius, the samples were randomly distributed from 90 mm to 110 mm. In this simulation, the total number of measurement points generated randomly was 267, which were projected into circles with a radial spacing of one millimeter and angular spacing of one degree. In order to resemble the parameter

settings of the real experiment shown in Section 3.3, in this Matlab simulation, the relative dielectric constant of the first, second, and third layer of the simulated three-layered C-SAR imaging structure was also set to $\varepsilon_r = 1$, $\varepsilon_r = 2.2$, and $\varepsilon_r = 2.4$, respectively. The point target was located at a position with a radius of 41.8 mm. As shown in Figure 2a, the PSF of the multi-layered circular dielectric structures SAR imaging in the non-uniform measurement case was well focused.
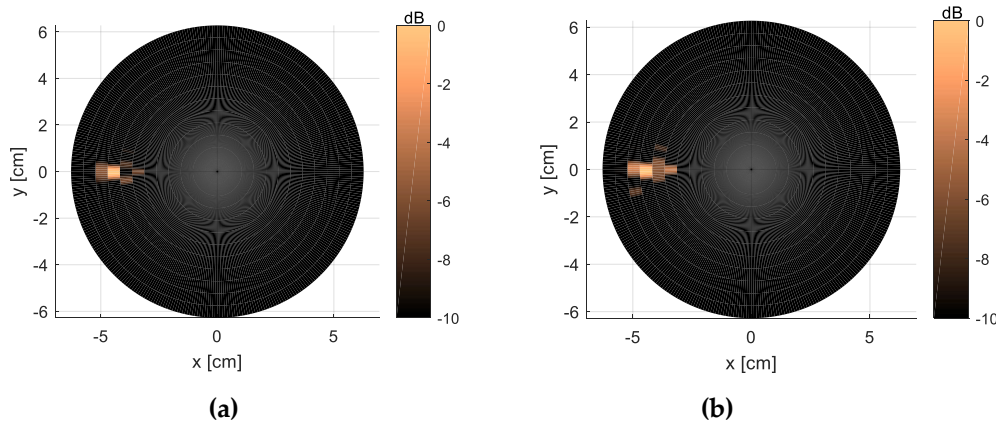
Figure 2. (**a**) Ideal point spread function (PSF) of 267 non-uniform measurement points in the Matlab simulation example; (**b**) Imaging result using the proposed method when random errors (include projection errors and location measurement errors) were introduced for the case of Figure 2a.

Moreover, in order to assess the robustness of the proposed imaging method with respect to projection errors and location measurement errors of the sampling points, random errors in the angular values and in the radius of measurement positions were introduced. In particular, random errors in the angular values were generated according to a uniform distribution between ±3 degrees, and random errors in the radii values were introduced according to a uniform distribution between ±5mm. The obtained results, including the random errors introduced to simulate projection errors and location measurement errors, are shown in Figure 2b. From these results, it is possible to see that, although the performance was slightly degraded with respect to the error-free case (Figure 2a), the impact of the introduced errors still provided good results. This showed that the proposed method was able to retrieve quality results, even in the presence of moderate positioning errors, making it suitable for practical applications.

In addition to the qualitative evaluation given by the previous figures, the quality of the proposed imaging method was also quantitatively studied by means of the integral side-lobe ratio (ISLR), which could be used as an effective indicator considering the ideal point target case. The ISLR is defined as the ratio between the energy of the main-lobe of the ideal point target in the image and the rest of the energy from the other parts of the imaging area. The ISLR of the images, shown in Figure 2a,b, was −6.14 dB and −8.50 dB, respectively.

Finally, the influence of the number of the acquisition was also studied by applying the algorithm considering 67 and 35 non-uniform measurement points generated randomly. In a similar fashion to the previous simulations, projection errors and location measurement errors were included in each acquisition point. The computed images considering 67 and 35 non-uniform measurement points could be observed in Figure 3a (ISLR = −10.98 dB) and Figure 3b (ISLR = −11.70 dB), respectively. As it could be seen, although the results obtained using 67 measurement points were worse than those obtained with 267 acquisitions, the point target could be clearly seen. Regarding the results obtained using 35 measurement points, some artifacts could be observed due to the under-sampling. At this

point, it is relevant to remark that in order to fulfill the sampling criterion in this type of cylindrical acquisition, the minimum sampling step along ϕ is given by [11]

$$\Delta\phi = \frac{\lambda}{4a_0} \tag{7}$$

where λ is the wavelength associated with the maximum working frequency, and a0 is the radius of the cylindrical target; in this case, it was 62.8 mm. In this case, the minimum sampling step along ϕ was 5.6°, which would require at least 65 measurement points considering uniformly spaced samples. Thus, artifacts could appear when undersampling, as confirmed by Figure 3b. In addition, it is also useful to note that using a sampling step under the Nyquist limit could be also beneficial as it helps to smooth the contribution of errors. Moreover, in real-measurements, it also helps to reduce the impact of noise.
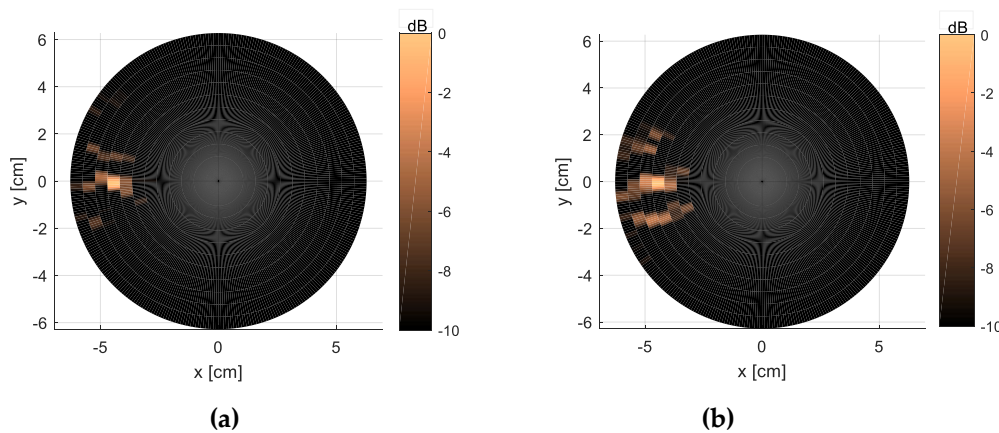

| (a) | (b) |

Figure 3. (**a**) Imaging result of 67 non-uniform measurement points using the proposed method when random errors (include projection errors and location measurement errors) were introduced; (**b**) Imaging result of 35 non-uniform measurement points using the proposed method when random errors (include projection errors and location measurement errors) were introduced.

3.2. CST Microwave Studio Simulation

In order to validate the proposed imaging method further, CST Microwave Studio® was used to generate the simulated echoed signal of multi-layered circular dielectric structures. These simulations were accomplished using wideband received signal data at 101 frequency points along the X-band frequency range (i.e., 8.2–12.4 GHz). The parameters of the CST model of the simulated multi-layered structure were selected to resemble the real experiment discussed in Section 3.3. The radii of the outer surface (second layer) and of the inner surface (the third layer) of the circular dielectric object were 115 mm and 85 mm, respectively. The polarization direction used in this simulation was parallel to the height direction axis of cylinders. The background medium (first layer) was assumed to be free space. As shown in Figure 4a, the measurement points were located in the angular range from $-\pi$ to π at a non-constant rate. Regarding the acquisition radius, the samples were randomly distributed from 170 mm to 190 mm. In this simulation, the total number of measurement points was 120.

The relative dielectric constant of the first, the second, and the third layer of this three-layer C-SAR imaging structure were $\varepsilon_r = 1$, $\varepsilon_r = 2$, and $\varepsilon_r = 4$-j0.01, respectively. In order to demonstrate the effectiveness of the proposed method, two small metallic cylinders, both with a radius of 2 mm and length of 20 mm, were considered as targets (see Figure 4b) to be detected. This cylindrical target geometry could be seen as an electrically small target (smaller than a quarter wavelength) along the circular cross-section. The cross-section of the simulated model, showing the position of both targets (which are in the inner layer), is depicted in Figure 4b. In particular, both targets were at 65 mm from the center of the cylinder, and the relative angular separation between them was 135 degrees. In order

to decrease the computational cost, the non-uniform measurement points, shown in Figure 4a, were only projected onto the circle, which had the shortest distance to them. In particular, 21 projection circles were considered with radii ranging between 170 and 190 mm with a 1 mm step size.
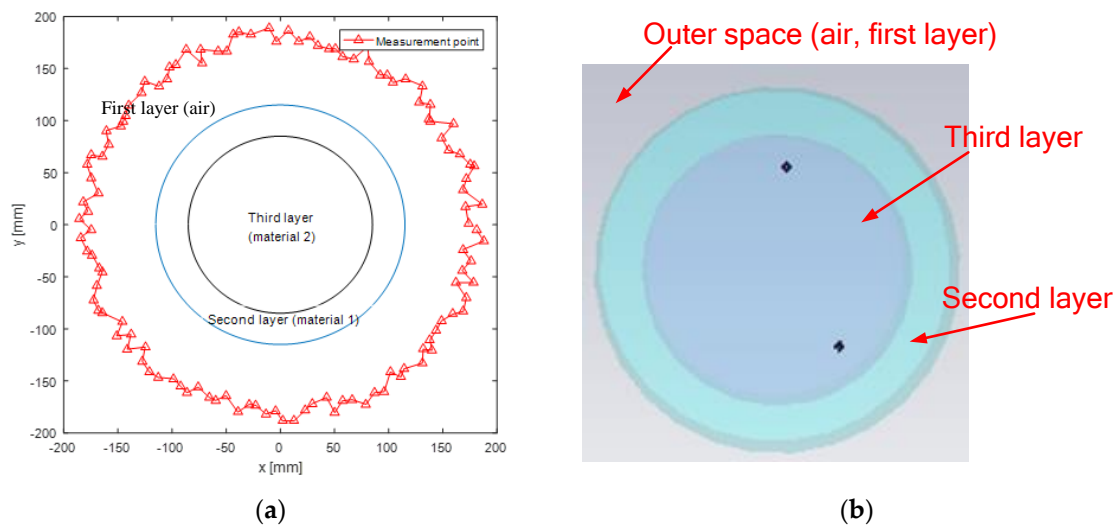

(**a**)

(**b**)

Figure 4. (**a**) Locations of the non-uniform measurement points. The radius of the acquisition points ranged from 170 mm to 190 mm; (**b**) CST Microwave Studio simulation model of two-point targets both located in the inner layer of the circular structure.

The final superposition SAR image of the simulated CST model, illustrated in Figure 4b, obtained from the non-uniform measurements with the positions shown in Figure 4a, is depicted in Figure 5a. In order to make a comparison with the uniformly sampled circular case, the SAR image of the same CST simulation model, using uniformly distributed measurements and considering a scanning radius of 180 mm, is shown in Figure 5b. In this case, the total number of measurement points was also 120.
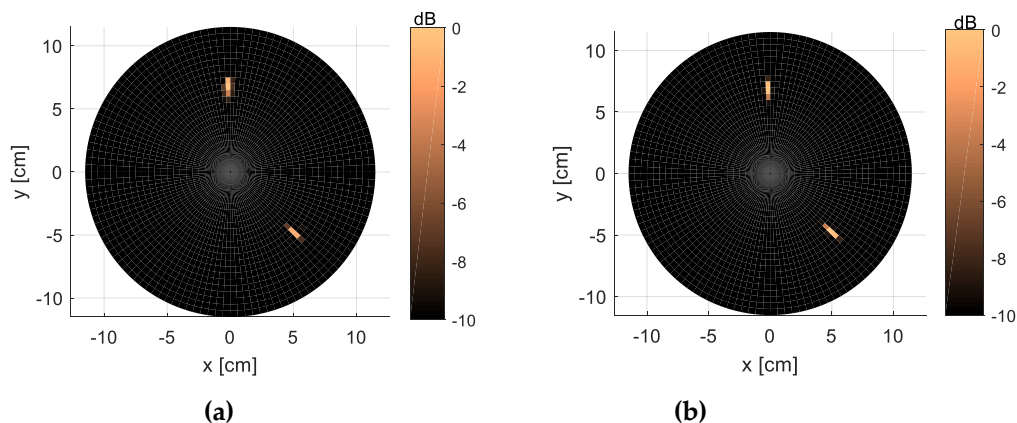

(**a**)

(**b**)

Figure 5. (**a**) Final superposition synthetic aperture radar (SAR) image of the CST simulation model, shown in Figure 4b, computed using non-uniform measurements acquired at the positions depicted in Figure 4a; (**b**) SAR image of the CST simulation model, depicted in Figure 4b, obtained from uniform measurements taken at a constant radius of 180 mm.

In Figure 5, the pixel which had the highest value was regarded as the location of the target. According to this criterion, both targets were at 67.5 mm from the center of the cylinder, and the relative angular separation between them was 135 degrees (Figure 5). The radius of the targets' location just had a little bias error (2.5 mm) compared to the ground truth value. This was caused by the sampling step size of the image. The sampling step size used in this CST simulation was 5 mm. The relative angular separation between the two targets was the same as the ground truth.

Moreover, in Figure 5, the comparison revealed that the focusing performance of the proposed imaging method was good, being the image quality comparable to that achieved in the case of uniformly distributed samples.

3.3. Real Experiment

In order to validate the performance of the proposed approach in a real environment, the setup shown in Figure 6a was used. In this setup, an open-ended rectangular waveguide (OEWG) was used to transmit and receive a continuous-wave stepped-frequency electromagnetic signal. The signal was generated by means of a vector network analyzer, which was acquiring the S11 parameter from 8.3 to 12.3 GHz at 201 frequency points. On the one hand, the OEWG was mounted on a robot-arm with the capability to move along the three-orthogonal axes (defined as xyz axes). On the other hand, the PVC pipe was put onto a turntable, which could be turned to any arbitrary measurement angle. Thus, the system enabled to simulate arbitrary acquisition angles and radii.
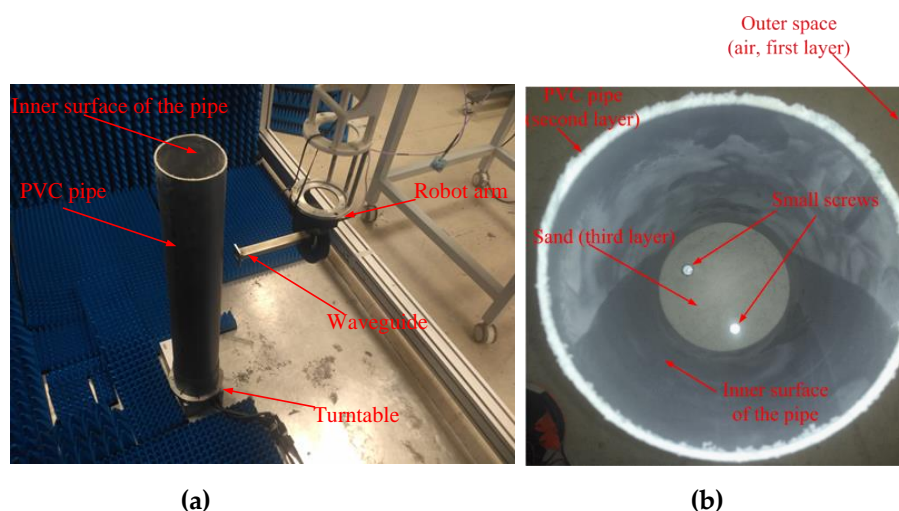

Figure 6. (**a**) Measurement setup; (**b**) Closer view of the polyvinyl chloride (PVC) pipe with the two screws before being completely covered by sand.

In this experiment, the targets were two screws located at the same height inside a PVC pipe full of sand. The head diameter, body diameter, and the height of the screws were 9.85 mm, 5.86 mm, and 22.16 mm, respectively. Regarding the pipe, the inner radius and the thickness were 59.3 mm and 3.5 mm, respectively. This geometry, together with the targets, is shown in Figure 6b, before being completely covered with sand. The relative dielectric constants of the PVC pipe and sand used in the real experiment at this band were 2.2 and 2.4, respectively. The S11 parameter was acquired at 1000 measurement points using a random angular step. As previously mentioned, this enabled to smooth the impact of positioning errors and noise. Regarding the radii, two experiments were accomplished for different radii. In the first one, the radii were also randomly generated at a range from 90 mm to 110 mm, whereas, in the second one, the radii were between 140 mm and 160 mm.

The final imaging results for this experiment, including also the results for the case of equally-spaced data for the sake of comparison (Figures 7b and 8b), are shown in Figures 7 and 8. In the uniformly-sampled circular cases, the scanned radii were set to 100 mm and 150 mm, respectively. As in the previous case, the depicted dynamic range in Figures 7 and 8 was also 10 dB. From Figures 7 and 8, the location of the targets could be clearly seen. In Figures 7 and 8, the two targets were at 50 and 40 mm from the center of the cylinder, respectively. The relative angular separation between them was 126 degrees. In Figure 6b, the ground truth values of the radii of the targets' location were both 46 mm. Similar to the CST simulation, this bias error in Figures 7 and 8 compared to the ground truth value was also mainly caused by the sampling step size of the image. The sampling step size used in this

experiment was 5 mm. The relative angular separation between the two targets was approximately the same as the ground truth, both in Figures 7 and 8. Both facts confirmed the accuracy of the proposed imaging method. It is relevant to note that, if compared with the theoretical PSF, the targets were slightly spread along the radial direction. The reason for this spread was that the targets also spread along the *z*-axis which is perpendicular to the 2D circular imaging slice and, therefore, the projection on the image plane resulted in this resolution reduction.
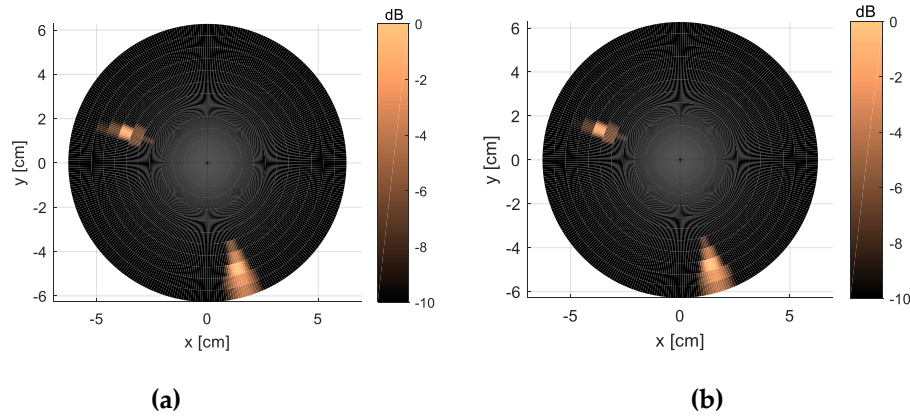

(a)   (b)

Figure 7. (**a**) Final superposition SAR image of the pipe measured at the experiment setup, shown in Figure 6, for the non-uniform measurement case when the scan radius ranged from 90 mm to 110 mm randomly; (**b**) SAR image of the same pipe computed using uniform measurements acquired at a constant radius of 100 mm.
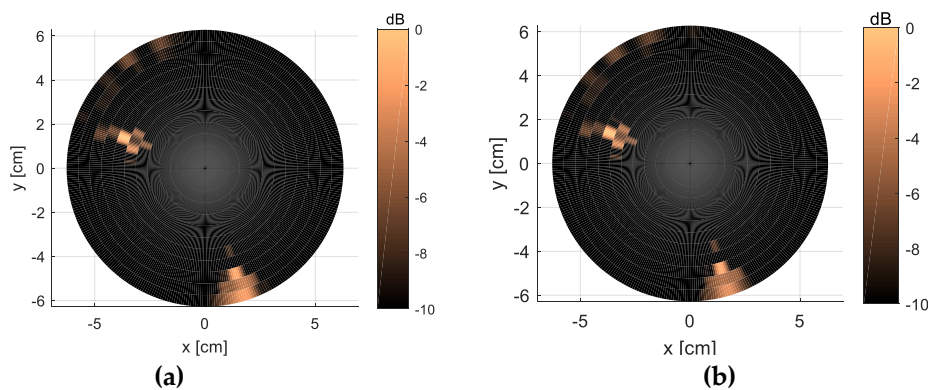

(a)   (b)

Figure 8. (**a**) Final superposition SAR image of the pipe measured at the experiment setup, shown in Figure 6, for the non-uniform measurement case when the scan radius ranged from 140 mm to 160 mm randomly; (**b**) SAR image of the same pipe computed using uniform measurements acquired at a constant radius of 150 mm.

Thus, similar to the simulations, the real experiment also demonstrated that the focused performance of the proposed imaging method was good enough.

4. Conclusions

In this paper, a method to solve the problem of multi-layered C-SAR imaging, using an algorithm based on Green's function and considering non-uniform measurement points, was proposed. For this purpose, the measurement points were projected onto different circles first, and then the SAR image of the imaging domain of each projection circle was obtained based on Green's function. The final SAR image was retrieved by the superposition of all sub-images based on each projection circle. Numerical and CST simulations and experimental results demonstrated the effectiveness and robustness of the proposed method for practical NDT applications. The proposed imaging method was not sensitive to

projection errors. Finally, it is noteworthy to mention that this method could be easily extended to other sampling schemes, such as 3D-cylindrical, in order to take into account the shape of targets along the *z*-axis, which is perpendicular to the 2D circular imaging slice.

Author Contributions: Conceptualization, B.W.; methodology, B.W., J.L.; software, B.W., J.L.; validation, B.W., J.L., G.Á.-N.; formal analysis, B.W., J.L.; investigation, J.L., G.Á.-N.; resources, J.L., G.Á.-N.; data curation, J.L., G.Á.-N.; writing—original draft preparation, B.W.; writing—review and editing, J.L., G.Á.-N.; visualization, B.W., J.L., G.Á.-N.; supervision, J.L.; project administration, J.L.; funding acquisition, B.W., J.L., G.Á.-N. All authors have read and agreed to the published version of the manuscript.

Conflicts of Interest: The authors declare no conflict of interest.

References

1. Soumekh, M. *Synthetic Aperture Radar Signal Processing*; Wiley: New York, NY, USA, 1999.
2. Soumekh, M. Reconnaissance with slant plane circular SAR imaging. *IEEE Trans. Image Process.* **1996**, *5*, 1252–1265. [CrossRef] [PubMed]
3. Dungan, K.E.; Potter, L.C. 3-D imaging of vehicles using wide aperture radar. *IEEE Trans. Aerosp. Electron. Syst.* **2011**, *47*, 187–200. [CrossRef]
4. Zhang, Z.; Lei, H.; Lv, Z. Vehicle Layover Removal in Circular SAR Images via ROSL. *IEEE Geosci. Remote Sens. Lett.* **2015**, *12*, 2413–2417. [CrossRef]
5. Bryant, M.L.; Gostin, L.L.; Soumekh, M. 3-D E-CSAR imaging of a T-72 tank and synthesis of its SAR reconstructions. *IEEE Trans. Aerosp. Electron. Syst.* **2003**, *39*, 211–227. [CrossRef]
6. Ponce, O.; Prats-Iraola, P.; Pinheiro, M.; Rodriguez-Cassola, M.; Scheiber, R.; Reigber, A.; Moreira, A. Fully polarimetric high-resolution 3-D imaging with circular SAR at L-band. *IEEE Trans. Geosci. Remote Sens.* **2014**, *52*, 3074–3090. [CrossRef]
7. Jia, G.; Buchroithner, M.F.; Chang, W.; Liu, Z. Fourier-based 2-D imaging algorithm for circular synthetic aperture radar: Analysis and application. *IEEE J. Sel. Top. Appl. Earth Obs.* **2016**, *9*, 475–489. [CrossRef]
8. Fallahpour, M.; Case, J.T.; Ghasr, M.T.; Zoughi, R. Piecewise and Wiener filter-based SAR techniques for monostatic microwave imaging of layered structures. *IEEE Trans. Antennas Propag.* **2014**, *62*, 282–294. [CrossRef]
9. Fallahpour, M.; Zoughi, R. Fast 3-D qualitative method for through-wall imaging and structural health monitoring. *IEEE Geosci. Remote Sens. Lett.* **2015**, *12*, 2463–2467. [CrossRef]
10. Jung, H.; Kim, K. Autofocusing Technique Based on Generalized Multilayer Stolt Migration. *IEEE Trans. Geosci. Remote Sens.* **2017**, *56*, 1386–1393. [CrossRef]
11. Laviada, J.; Wu, B.; Ghasr, M.T.; Zoughi, R. Nondestructive Evaluation of Microwave-Penetrable Pipes by Synthetic Aperture Imaging Enhanced by Full-Wave Field Propagation Model. *IEEE Trans. Instrum. Meas.* **2019**, *68*, 1112–1119. [CrossRef]
12. Wu, B.; Gao, Y.; Laviada, J.; Ghasr, M.T.; Zoughi, R. Time-Reversal SAR Imaging for Nondestructive Testing of Circular and Cylindrical Multi-Layered Dielectric Structures. *IEEE Trans. Instrum. Meas.* **2019**. [CrossRef]
13. Moon, H.; Teixeira, F.L.; Donderici, B. Stable pseudoanalytical computation of electromagnetic fields from arbitrarily-oriented dipoles in cylindrically stratified media. *J. Comput. Phys.* **2014**, *273*, 118–142. [CrossRef]
14. Moon, H.; Donderici, B.; Teixeira, F.L. Stable evaluation of Green's functions in cylindrically stratified regions with uniaxial anisotropic layers. *J. Comput. Phys.* **2016**, *325*, 174–200. [CrossRef]
15. He, H.; Maheshwari, P.; Pommerenke, D.J. The development of an EM-field probing system for manual near-field scanning. *IEEE Trans. Electromagn. Compat.* **2016**, *58*, 356–363. [CrossRef]
16. Laviada, J.; Ghasr, M.T.; Lopez-Portugues, M.; Las-Heras, F.; Zoughi, R. Real-Time Multiview SAR Imaging Using a Portable Microwave Camera With Arbitrary Movement. *IEEE Trans. Antennas Propag.* **2018**, *66*, 7305–7314. [CrossRef]

17. Álvarez-Narciandi, G.; López-Portugués, M.; Las-Heras, F.; Laviada, J. Freehand, Agile, and High-Resolution Imaging With Compact mm-Wave Radar. *IEEE Access* **2019**, *7*, 95516–95526. [CrossRef]